Available online at www.sciencedirect.com

jmr&t Journal of Materials Research and Technology

journal homepage: www.elsevier.com/locate/jmrt

Original Article

Superior dynamic shear properties and deformation mechanisms in a high entropy alloy with dual heterogeneous structures

Shuang Qin [a], *Muxin Yang* [a], *Yanke Liu* [a,b], *Ping Jiang* [a], *Jitang Fan* [c], *Fuping Yuan* [a,b,*], *Xiaolei Wu* [a,b]

[a] *State Key Laboratory of Nonlinear Mechanics, Institute of Mechanics, Chinese Academy of Sciences, 15 Beisihuan West Road, Beijing 100190, China*

[b] *School of Engineering Science, University of Chinese Academy of Sciences, 19A Yuquan Road, Beijing 100049, China*

[c] *State Key Laboratory of Explosion Science and Technology, Beijing Institute of Technology, Beijing 100081, China*

ARTICLE INFO

Article history:
Received 24 March 2022
Accepted 8 June 2022
Available online 21 June 2022

Keywords:
High-entropy alloys
Heterogeneous structures
Precipitates
Strain hardening
Adiabatic shear band
Dynamic properties

ABSTRACT

Both heterogeneous grain structure and dual nanoprecipitates were designed in a $Al_{0.5}Cr_{0.9}FeNi_{2.5}V_{0.2}$ high entropy alloy (HEA), and the dynamic shear responses were investigated by hat-shaped specimens in split Hopkinson pressure bar tests. The present HEA with heterogeneous structure displays an unprecedented synergy of dynamic shear strength and ductility, as compared to the literature data for other metals and alloys. The excellent dynamic shear properties in the unaged samples could be due to the dynamical grain refinement, the dislocations hardening, and the precipitation hardening. The aged samples with a higher volume fraction of coherent $L1_2$ nanoprecipitates display even better dynamic shear properties, as compared to the unaged samples, which can be attributed to the triggered planar dislocation slip, the stored higher density of dislocations, the formation of dislocation substructure and the more pronounced precipitation hardening for postponing the occurrence of the adiabatic shear band (ASB). The high strain rate, high strain/stress magnitude, high adiabatic temperature rise, and fast-cooling process within ASB were observed to induce the dynamic recrystallization and the phase transformation from FCC phase to B2 phase, and this newly observed phase transformation phenomenon was not observed before under quasi-static deformation conditions.

1. Introduction

Adiabatic shear band (ASB), which is generally defined as a narrow deformation band with highly localized strain and high adiabatic temperature rise, is the major failure mode for metals and alloys under high strain rate impact loading [1–8]. Formation of ASB generally accompanies the fast loss of load-carrying capacity of materials, regarded as a precursor of final catastrophic failure [9–11]. In other words, this plastic

* Corresponding author.
E-mail address: fpyuan@lnm.imech.ac.cn (F. Yuan).

https://doi.org/10.1016/j.jmrt.2022.06.074

deformation failure mode extremely threatens the safety service of structural materials under high strain-rate conditions. Until now, extensive efforts have been carried out to investigate the formation of the ASB [3–5,12,13]. It is widely accepted that the local plastic instability within shear bands can be activated when the thermal softening effect overwhelms the strain hardening ability of metals or alloys, suggesting that the materials with a good combination of strength and ductility can effectively retard the initiation of ASB. However, in conventional metals or alloys, the strength and ductility are mutually exclusive in nature [14].

High-entropy alloys (HEAs) [15–19] and medium-entropy alloys (MEAs) [20–23] as a class of the most promising materials to emerge in recent years, which contain multiple principal elements in equimolar or near equimolar ratios. Recently, CoCrNi MEA and FeCrMnCoNi HEA with a single Face-Centered Cubic (FCC) phase have displayed superior tensile and fracture properties at room temperature, and even better mechanical properties at cryogenic temperature due to a transition of deformation mechanism [24,25]. However, single FCC phase MEAs/HEAs with coarse grains show a relatively low strength, which severely impedes practical applications. The strength of single-phase MEAs or HEAs can be significantly improved by severe plastic deformation, by which high dislocation density and grain refinement can be simultaneously achieved. However, such elevated strength is at an expense of ductility in the homogeneous structure [26]. It is shown that the design strategy of elaborately tailoring heterogeneities in microstructures can overcome the strength-ductility trade-off dilemma, due to the incompatible deformation between the soft domains and the hard domains [27–31]. The incompatible deformation can lead to the generation of geometrically necessary dislocations (GNDs), as well as the stress/strain partitioning [32,33]. For example, the CoCrNi with heterogeneous grain structure exhibits a noticeable improvement in the synergy of strength and ductility, mainly due to the extra hetero-deformation induced (HDI) hardening [33]. Additionally, the second-phase particle formed in MHAs/HEAs is another essential hardening strategy. However, the hard intermetallic compound has not been considered in the early stage of MEA/HEA development since the second-phase particle was generally considered to be brittle and detrimental to ductility [15,16,24]. In the recently reported studies [34–37], the second-phase particles, especially at the nanoscale and with coherent boundaries, can achieve excellent strength without sacrificing ductility. The dislocations need extra shear stress to cut through the shearable coherent precipitates or bow out/bypass the non-shearable precipitates, thus the strength can be significantly improved. Meanwhile, the uniform distribution of nano-sized precipitates can effectively suppress or alleviate the strain localization. It is noted that only the second-phase precipitates with appropriate size, shape and dispersion can reach a favorable combination of strength and ductility.

The dynamic properties of several representative MHAs/HEAs with homogeneous structures have been reported in recent studies, exhibiting the exceptional dynamic shear property under cryogenic temperature, the excellent resistance to hydrogen embrittlement failure, the outstanding self-sharpening penetration capacity, as well as the high ballistic resistance ability [38–41]. Although the quasi-state mechanical behaviors of the HEAs/MEAs with heterogeneous microstructures have been extensively investigated, their dynamic shear response was still limited. Moreover, the impact response of HEAs/MEAs with dual-heterogeneous structures (heterogeneous grain structures and nanoprecipitates) has not been explored yet, and the HEAs/MEAs with dual-heterogeneous structures have great potential to attain excellent dynamic properties. In this regard, the $Al_{0.5}Cr_{0.9}FeNi_{2.5}V_{0.2}$ alloy has been employed as the experimental material, dual-heterogeneous structures with heterogeneous grain structures and $L1_2$/B2 precipitates can be obtained in such HEA according to our previous study [42]. A series of dynamic shear tests have been performed on the hat-shaped specimens, using the split Hopkinson pressure bar (SHPB). Due to the geometry of a hat-

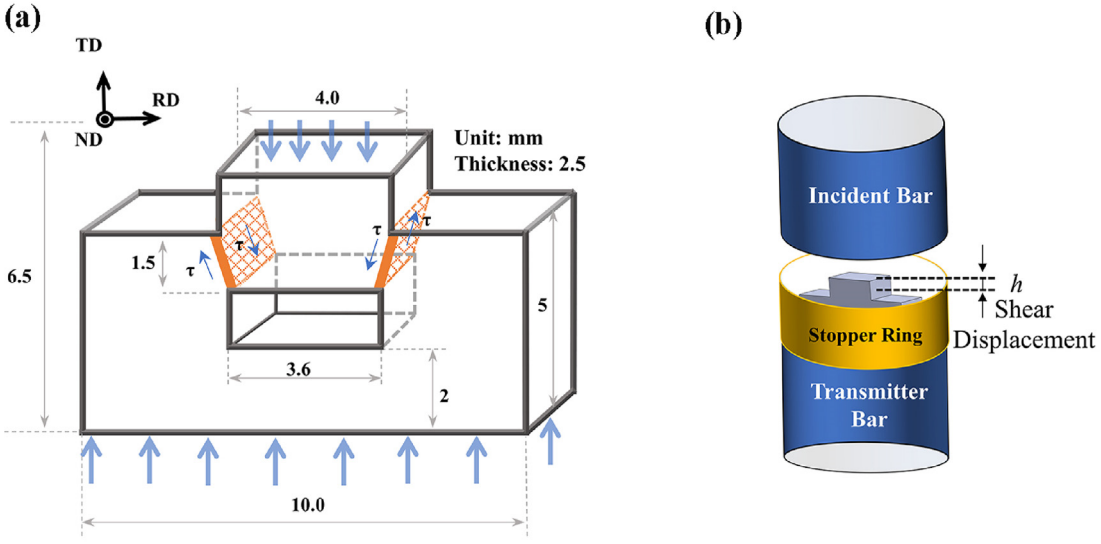

Fig. 1 – Schematic diagrams of (a) the hat-shaped specimen and (b) the interrupted test controlled by a stopper ring in the Hopkinson pressure bar experiment.

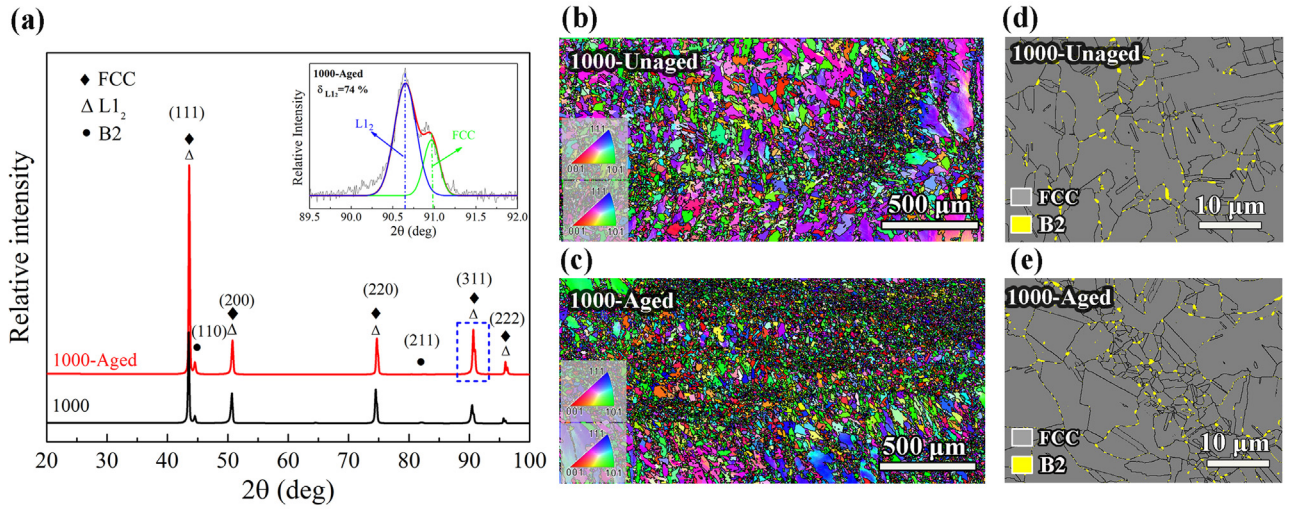

Fig. 2 – Microstructural characterizations by XRD and EBSD for one typical annealed sample (1000-Unaged) and one typical aged sample (1000-Aged) prior to the dynamic testing. (a) XRD spectra (the inset shows the typical asymmetric peaks of (311) plane corresponding to FCC and $L1_2$ phases). IPF images for: (b) 1000-Unaged sample; (c) 1000-Aged sample. EBSD phase maps revealing the distribution of B2 precipitates in the FCC matrix for (d) 1000-Unaged sample and (e) 1000-Aged sample.

shaped specimen, the strain localization or the adiabatic shear failure is predetermined at a specific region which facilitates the microstructural observations. Moreover, the interrupted shear tests have been utilized to capture the evolution of microstructures associated with plastic deformation. The microstructural mechanisms of the macroscopical dynamic shear properties have been revealed. Then, the influences of heterogeneous grain structures and nanoprecipitates on the dynamic shear behaviors, as well as the strain hardening mechanisms have been elucidated.

2. Materials and methods

2.1. Materials preparation

The $Al_{0.5}Cr_{0.9}FeNi_{2.5}V_{0.2}$ ingots were fabricated in an arc-melting furnace under an argon atmosphere (the purity of each raw material was larger than 99.9%), and then re-melted five times to ensure the chemical homogeneity. The as-cast alloys were homogenized at 1200 °C for 24 h followed by water quenching, and then gradually cold-rolled in steps at room temperature with an initial thickness of 8 mm. Finally, the as-rolled sheets with a thickness of about 2.5 mm were further subjected to heat treatments for obtaining various heterogeneous microstructures. Specifically, the sheets were first annealed at temperatures of 850–1200 °C for 20 min followed by water quenching (these samples are specified as 850-Unaged, 900-Unaged, 1000-Unaged, 1100-Unaged, and 1200-Unaged, respectively), and then aged at 600 °C for 1 h followed by water quenching (these samples are specified as 850-Aged, 1000-Aged, 1100-Aged, and 1200-Aged, respectively).

2.2. Mechanical testing methods

The hat-shaped plate specimens were machined by a wire electrical discharge machine, the dimension of the specimen is shown in Fig. 1(a). The topmost plane of the hat-shaped specimen is the onset of impact loading, and the impact loading direction is parallel to the transverse direction (TD) of the specimen. All specimens were polished in advance to eliminate surface irregularities. The hat-shaped specimen was firstly proposed by Meyer et al. [43], by which the high-strain shear deformation is concentrated in a narrow and pre-determined region, as marked by the orange areas in Fig. 1(a).

The dynamic shear experiments were performed at a strain rate of approximately 5.0×10^4 s^{-1} employing the SHPB apparatus. During the impact experiment, the specimen was sandwiched between the incident and transmitter bars, as shown in Fig. 1 (b), and the initial voltages were recorded by a data acquisition system. According to the one-dimensional elastic stress wave theory, the shear stress (τ), shear strain (γ), and strain rate ($\dot{\gamma}$) can be calculated as [9,43].

$$\tau = E\left(\frac{A}{A_s}\right)\varepsilon_T \tag{1}$$

$$\gamma = \frac{2C_0}{\delta}\int_0^t \varepsilon_R dt \tag{2}$$

$$\dot{\gamma} = \frac{2C_0}{\delta}\varepsilon_R \tag{3}$$

where E, A, and C_0 are Young's modulus (210 GPa), the cross-sectional area of bar (132.7 mm^2), and longitudinal elastic wave velocity (5050 m/s), respectively. A_s is the cross-sectional area and δ is the thickness of the localized shear region. ε_R and ε_T represent the reflected and transmitted strain signals recorded by the strain gages, respectively.

A series of interrupted "frozen" experiments were performed on 1000-Unaged and 1000-Aged specimens to investigate the microstructure evolution in the concentrated deformation region, using the maraging steel stopper ring to

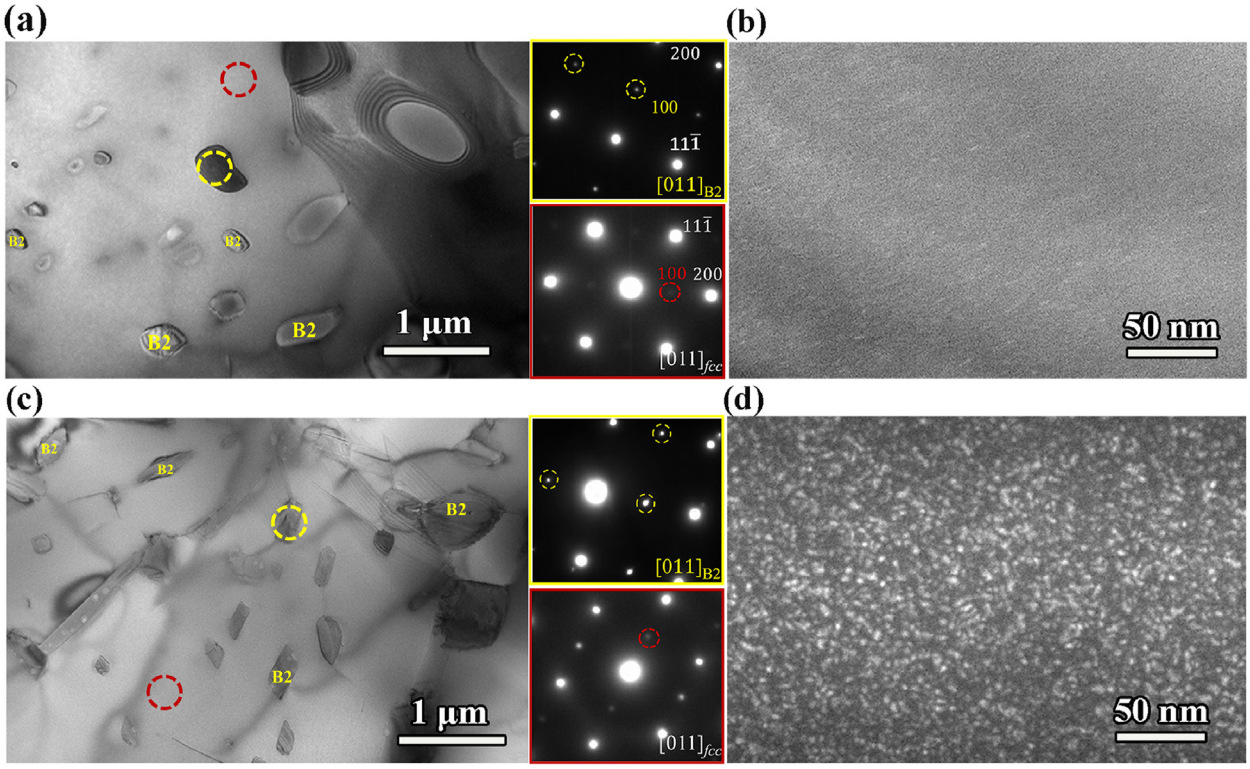

Fig. 3 – TEM micrographs for 1000-Unaged and 1000-Aged samples, respectively. (a) and (c) Bright-field images, where the B2 phase (yellow circles) and FCC matrix (red circles) are identified by SAED patterns in the insets. (b) and (d) Dark-field images revealing the distributions of $L1_2$ nanoprecipitate in the FCC matrix.

control the final displacement of sample *h*, as shown in Fig. 1(b). The other details for dynamic shear tests can be found in our previous research [38].

2.3. *Microstructural characterization*

The microstructures of specimens before and after dynamic shear tests were characterized by X-ray diffraction (XRD), electron back-scattered diffraction (EBSD) and transmission electron microscopy (TEM), and high-resolution TEM (HRTEM). In specific, phase identification of the specimen was performed by XRD using Cu Kα radiation with a scanning 2θ range of 20-100° and a step size of 0.01°. The EBSD observation was conducted by the Zeiss Gemini scanning electron microscope 300 equipped with the Oxford Symmetry S2 detector, and the post-processing Oxford Instruments Aztec 2.0 EBSD system software (Channel 5 software) was used, and the step size was set to be 0.08 or 2 μm. The microstructural TEM and HRTEM observations were conducted by the JEOL 2100F TEM equipment operated at a voltage of 200 kV. Moreover, thin foils for the TEM and HRTEM analyses were first mechanically ground to a thickness of 45 μm and subsequently thinned by a twin-jet polishing facility with 95% ethanol and 5% perchloric acid solution under −30 °C and 30 V conditions. A more detailed description of sample preparations can be found elsewhere [44].

3. Results and discussions

3.1. *Microstructural characterizations prior to dynamic shear testing*

XRD results indicate that the 1000-Unaged and 1000-Aged specimens have B2 and $L1_2$ precipitates in the FCC matrix, as shown in Fig. 2(a), in which the peaks corresponding to the FCC, B2 and $L1_2$ phases are marked respectively for clarity. Since the lattice parameters of FCC and $L1_2$ phases are very similar, their fundamental peaks are almost overlapped in the XRD patterns. In this case, using the diffraction peak of the asymmetric (311) plane as an example, we employed the Gaussian fitting function to deconvolute the overlapped peaks [45]. As indicated from the inset of Fig. 2(a) for the 1000-Aged specimen, the high-intensity blue peak represents the $L1_2$ phase and the relatively low-intensity green peak stands for the FCC phase. The integrated peak intensity *I* for each peak can be used to estimate the volume fraction of each phase *v* ($I_{L1_2}/I_{FCC} = (F^2_{L1_2}/F^2_{FCC}) \times (v_{L1_2}/(1 - v_{L1_2}))$), and the square ratio of the structure factors for $L1_2$ and FCC phases ($F^2_{L1_2}/F^2_{FCC}$) was considered to be 1 [45]. Thus the relative volume fraction of the $L1_2$ phase could be estimated to be about 74% for the 1000-Aged specimen which is much higher than that in the 1000-Unaged specimen (14%). The inverse pole figure (IPF) of the

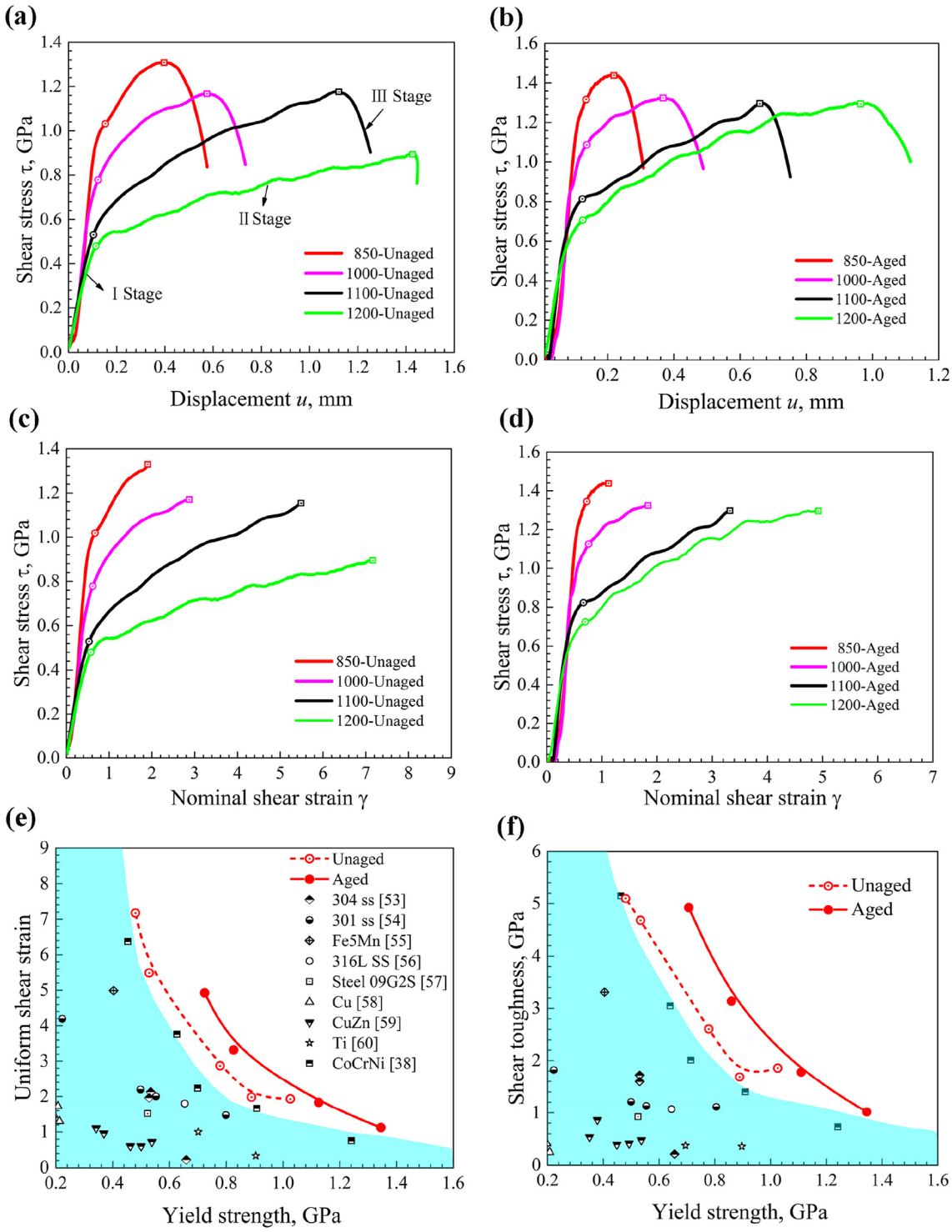

Fig. 4 – Dynamic shear properties. Shear stress as a function of shear displacement for (a) the unaged samples and (c) the aged samples. Shear stress as a function of nominal shear strain for (b) the unaged samples and (d) the aged samples. (e) Uniform shear strain as a function of dynamic shear yield strength and (f) shear toughness as a function of dynamic shear yield strength for all tested samples, along with the data for other metals and alloys.

1000-Unaged and 1000-Aged specimens are shown in Fig.2(b) and (c), respectively. Both specimens show bimodal microstructures, in which the recrystallized submicron grains are embedded in the coarse grains. Based on the EBSD observations, the average grain size is estimated to be 19.1 and 18.2 μm for the 1000-Unaged and 1000-Aged samples, respectively. It is noted that the aged sample exhibits a relatively smaller grain size than that of the unaged sample,

possibly since the nanoprecipitate inhibits the grain growth due to the increased difficulty for grain nucleation according to the Gibbs–Thomson equation [46].

Moreover, the close-up phase maps for the Unaged and Aged samples are displayed in Fig. 2(d) and (e). B2 particles are observed to preferentially precipitate along the high-angle grain boundaries (GBs), especially enriching at the triple-junction regions. Based on XRD and EBSD results, the volume fraction of B2 phase is similar in both samples (5% vs. 8% for 1000-Unaged and 1000-Aged specimens).

The morphology and distribution of precipitates in the abovementioned two samples were further investigated by TEM images, as shown in Fig. 3. The selected area electron diffraction (SAED) patterns from the [011] zone axis substantiate the existence of ordered $L1_2$ and B2 precipitates. Moreover, the recrystallized grain interior is relatively clean indicating a

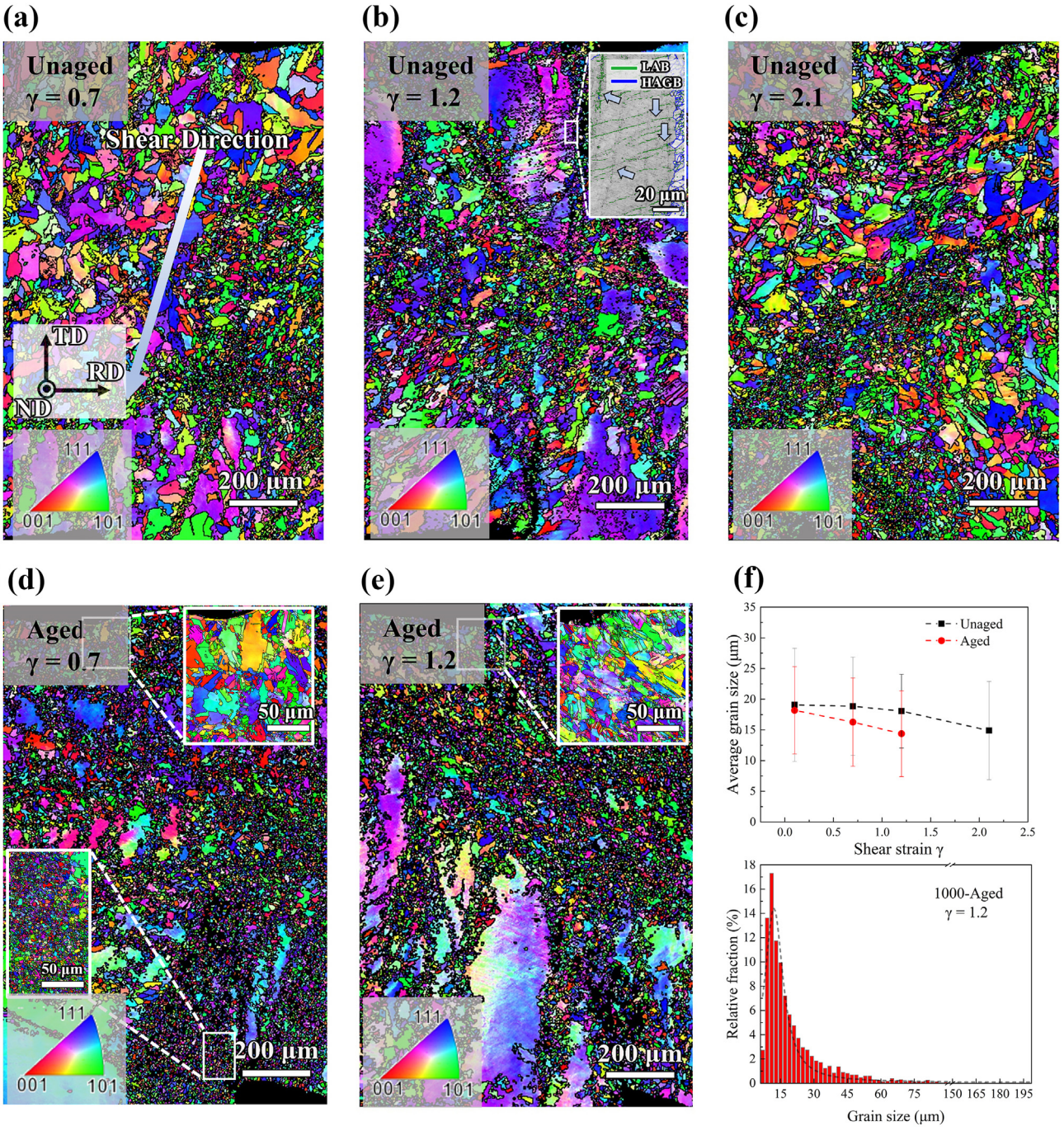

Fig. 5 – Microstructural evolutions by IPF maps at various controlled shear strains for typical samples. (a)–(c) IPF maps of the 1000-Unaged sample at the shear strains of 0.7,1.2 and 2.1, respectively. (d)–(e) IPF maps of the 1000-Aged sample at shear strains of 0.7 and 1.2, respectively. (f) The average grain size in the shear zone as a function of the shear strain for both samples and the histogram distribution of grain size for the 1000-Aged sample at a shear strain of 1.2.

low density of dislocation, and B2 particles with a grain size ranging from several hundred nanometers to one micrometer are observed in both samples, as shown in Fig. 3(a) and (c). The relative volume fractions of B2 phase for the samples of 1000-Unaged and 1000-Aged are estimated to be about 6% and 10%, respectively, which are close to the results for the EBSD observations. Additionally, the superlattice spots in the $[011]_{fcc}$ diffraction pattern indicate the evidence of ordered $L1_2$ phases, as well as the coherent relationship between $L1_2$ precipitate and FCC matrix. However, the superlattice spots are quite weak in the 1000-Unaged sample, possibly due to the lower volume fraction of $L1_2$ phase and the sluggish ordering kinetics [47], which leads to the low degree of long-range order of the $L1_2$ structure. The corresponding dark-field TEM images taken are presented in Fig. 3(b) and (d). It is indicated that the coherent ordered $L1_2$ precipitates in several nanometers size are uniformly distributed in the matrix. Moreover, the $L1_2$ precipitates in the 1000-Aged sample have a much coarser size and higher volume fraction compared to the corresponding unaged one. The relative volume fractions of $L1_2$ phase for the samples of 1000-Unaged and 1000-Aged are estimated to be about 13% and 69%, which are very close to the XRD results. Meanwhile, the distribution of network-like $L1_2$ precipitate substantiates the FCC/$L1_2$ structure formed via the spinodal decomposition [48]. It is therefore concluded that the subsequent aging treatment does not alter the volume fraction of B2 phase, but obviously increase the size and volume fraction of $L1_2$ phase.

3.2. Dynamic shear responses

The dynamic shear tests were conducted for various samples to examine the microstructure effects on mechanical responses. The shear stress–displacement curves for the unaged samples and the aged samples are presented in Fig. 4(a) and (c), respectively. All curves follow the same trend, and the minor fluctuation in curves is associated with the wave dispersion effect in Hopkinson bars.

Three stages are observed for these curves: (i) Dynamic shear stress is observed to increase linearly and dramatically fast with increasing shear displacement in the first elastic stage; (ii) The shear stress is found to steadily grow up to the peak value in the second stage; (iii) The shear stress starts to drop due to the formation of ASB in the third stage. The relation of the shear stress τ and shear strain γ can be mathematically described by [49].

$$\frac{d\tau}{d\gamma}=\left(\frac{\partial\tau}{\partial\gamma}\right)_{\dot{\gamma},T}+\left(\frac{\partial\tau}{\partial\dot{\gamma}}\right)_{\gamma,T}\frac{d\dot{\gamma}}{d\gamma}+\left(\frac{\partial\tau}{\partial T}\right)_{\gamma,\dot{\gamma}}\frac{dT}{d\gamma} \quad (4)$$

Where the first and second terms represent the hardening effects (strain or strain-rate) while the last term refers to the thermal softening effect (T is the absolute temperature within the ASB). Hence, dynamic shear stress–displacement curves are reflections of competition between the hardening effect and the thermal softening effect. In the second stage, the hardening effect transcends the thermal softening effect ($d\tau/d\gamma>0$). While the thermal softening effect overwhelms the hardening effect in the third stage ($d\tau/d\gamma\leq 0$), resulting in the thermo-viscoplastic instability and formation of ASB after the maximum stress point.

The uniform shear stress–strain curves can be seen in Fig. 4(b) and (d). The results exhibit that the ultimate uniform shear strain of specimens increases as the annealing temperature increases, while the maximum shear stress decreases with an increasing annealing temperature. Specifically, when the annealing temperature ranges from 1200 to 850 °C, the ultimate uniform shear stress increases from 634 to 1329 MPa (an increment of nearly 110%). While an ultimate shear strain reaches up to 7 for the specimen annealed at 1200 °C. It is suggested that the formation of ASB is strongly dependent on the microstructure of specimens. It is well known that FCC metals with coarse grains possess excellent tensile ductility and strong strain hardening due to the forest-dislocation hardening and the deformation twinning effects [50,51]. In addition, the increase in annealing temperature significantly facilitates grain growth. Thus, the specimen with a large grain size possesses a high resistance to localized deformation.

As compared to the conventional alloys, it is well accepted that HEAs need higher thermal energy to break atomic bonds due to the sluggish diffusion effect [52]. Thus, it is concluded that the HEAs with a strong hardening ability and a temperate thermal softening effect, resulting in a large plastic deformation as well as a high dynamic yield strength, as can be seen from Fig. 4(e) and (f). It is observed that the present HEA with heterogeneous structures has a superior dynamic shear property, as compared to all metals and alloys tested before [38,53–60]. It is also worth noting that the aged samples have an excellent combination of shear yield strength and impact shear toughness/uniform shear strain in comparison with the unaged counterparts. As indicated previously, the heterogeneity of the microstructure for the aged samples is severer due to the higher volume fraction of the coherent ordered $L1_2$ nanoprecipitate, as compared to that for the unaged samples. Hence, to unveil the original excellent dynamic properties in the aged samples, the microstructural evolution of ASB by the interrupted tests using stopper rings, as well as the dynamic deformation mechanisms will be systematically discussed.

3.3. Microstructural mechanisms for superior dynamic shear properties

In order to reveal the microstructural evolution of the samples during dynamic shear conditions, the “frozen” tests were performed on the 1000-Unaged and 1000-Aged samples at the various levels of uniform shear strain (0.7, 1.2, and 2.1).

The IPF maps for the 1000-Unaged sample at three different interrupted shear strains and the IPF maps for the 1000-Aged sample at two different interrupted shear strains are presented in Fig. 5(a)–(e), respectively. The step size was set to be small enough to identify the FCC grains and provide kernel average misorientation (KAM) maps. The resolved area fraction is about 82% even after severe shear deformation. Since the initiation of ASB or fracture crack is not observed at these specific shear strains, it can be assumed that the plastic deformation is homogeneous along the shear direction. Specifically, the image with low-angle and high-angle GBs is shown in the inset of Fig. 5(b), it is shown that the deformation substructures (such as low angle GBs, marked by arrows) are

formed in the grain interior of the coarse grain to accommodate the plastic deformation. These low-angle GBs can also be reflected by the generation of the in-grain small orientation gradient, as indicated by Fig. 5(b). Moreover, grain refinement is observed with respect to the increasing shear strains for both samples. The close-up views of the tip regions are shown in the insets of Fig. 5(d) and (e), in which the grains are severely distorted and elongated along the shear direction.

Moreover, the corresponding KAM maps at various shear strains are presented in Fig. 6(a)–(e). KAM is the variation of local orientation, regarding the average misorientation of one point with respect to the first nearest neighboring points in a grain. KAM value can be utilized to assess the extent of local plastic strain distribution, and further evaluate the density of GNDs according to the strain gradient theory [61]. It is observed that the plastic deformation concentrates in the bandlike area, as delineated by the dash lines in Fig. 6(a). A high density of GND is found at GBs due to the high strain gradient induced by the plastic deformation incompatibility across these interfaces, as indicated by the arrows in the inset

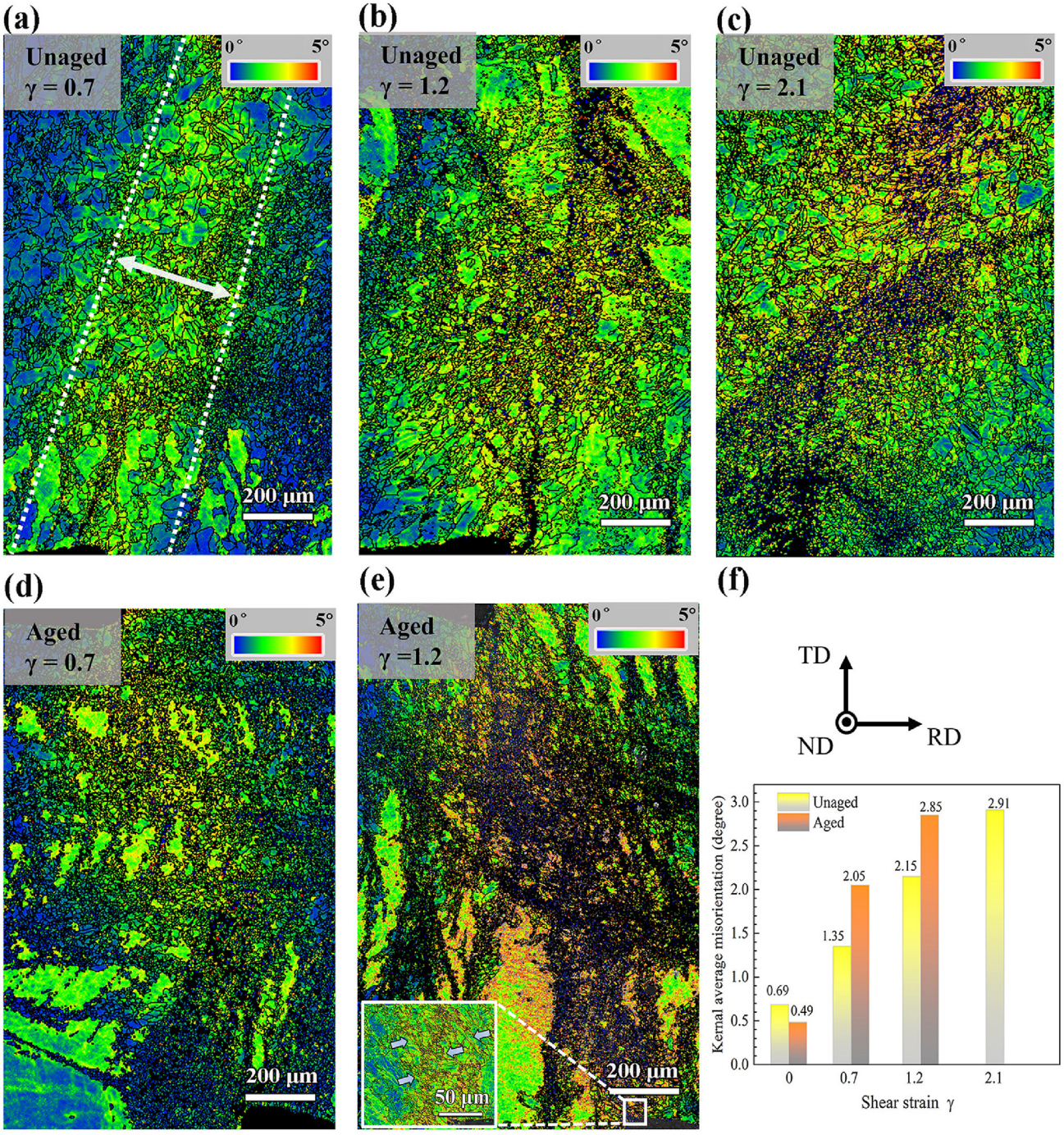

Fig. 6 – Microstructural evolutions by KAM maps at various controlled shear strains. (a)–(c) KAM maps for the 1000-Unaged sample at the shear strains of 0.7,1.2 and 2.1, respectively. (d)–(e) KAM maps for the 1000-Aged sample at the shear strains of 0.7 and 1.2, respectively. (f) The average KAM value in the shear zone as a function of the shear strain for both samples.

of Fig. 6(e). Figs 5(f) and 6(f) present the average grain size and KAM value in the shear zone under different shear strains for both samples. The average KAM value increases gradually while the grain size decreases with the increasing shear strains for both samples. Furthermore, at the same shear strain level, the 1000-Aged specimen shows a relatively higher KAM value as compared to the 1000-Unaged specimen. These observations demonstrate that the aged samples produce a high density of GND, leading to the strong hetero-deformation-induced (HDI) strengthening/hardening contribution [21]. Specifically, the average grain size gradually decreases from 18 to 14 μm in the 1000-Aged specimens as the shear strain reaches up to 1.2. At the same shear strain, the average grain size in the 1000-Aged specimen is relatively lower than that in the 1000-Unaged specimen. Thus, the excellent dynamic shear properties in the aged samples can be mainly attributed to the more efficient dynamic grain refinement and the higher contributions of HDI strengthening/hardening, as compared to the unaged samples.

In order to further elucidate the plastic deformation mechanisms, a series of representative TEM images for the 1000-Unaged and 1000-Aged specimens at the same shear strain level are displayed in Fig. 7 (along the <011> zone axis of FCC). For the 1000-Unaged specimen at a shear strain of 1.2, high-density non-planar dislocations are observed in the coarse grain interior, as indicated in Fig. 7(a). In contrast, for the 1000-Aged specimen, the uniformly dispersed planar dislocations are observed in the grain interior, as shown in Fig. 7(c) and (d) [62,63]. In such a deformation substructure, the dislocation storage capacity can be increased due to the intersections of planar dislocations. It is well accepted that the critical back stress forced on the dislocation source will activate other slip planes to accommodate further plastic deformation (as indicated in Fig. 7(c) and (d)) when the number of dislocations on the first slip plane reaches a saturation [64]. High-density dislocation accumulations around the B2 particles are found in Figs.7(b) and (d), in which numerous dislocations are blocked by the hard B2 nano-particles. It is indicated that the hard B2 nano-particles are very efficient on pinning the dislocations for the by-pass or Orowan-type strengthening/hardening, leading to excellent dynamic properties.

It is widely accepted that the arrangement of dislocations is primarily controlled by the stacking fault energy as well as the activation energy for cross-slip [63]. Since the planar slip planes are observed in the 1000-Aged sample, it is suggested that the uniformly dispersed coherent $L1_2$ nanoprecipitate may be beneficial to triggering the multiple slip planes in the FCC matrix under the high strain-rate condition. Associating with the glide plane softening effect, the destruction of shearable nanoprecipitate can extremely facilitate the dislocation movements and the formation of dislocation substructure under the quasi-static conditions [64]. Thus, under the dynamic loading condition, the present and the higher

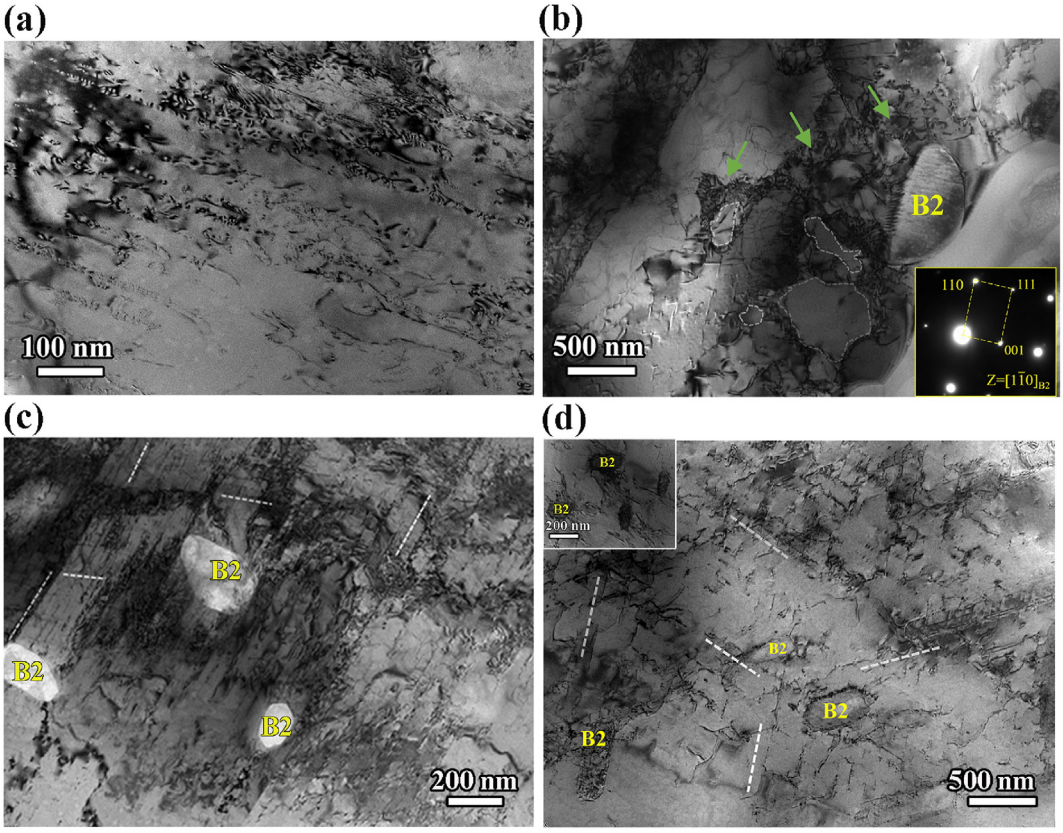

Fig. 7 – TEM morphologies of the deformed microstructures at a shear strain of 1.2. (a) (b) For 1000-Unaged specimen. (c) (d) For 1000-Aged specimen. The inset of (b) indicates the B2 phase and the inset of (d) reveals the interactions of dislocations with B2 particles.

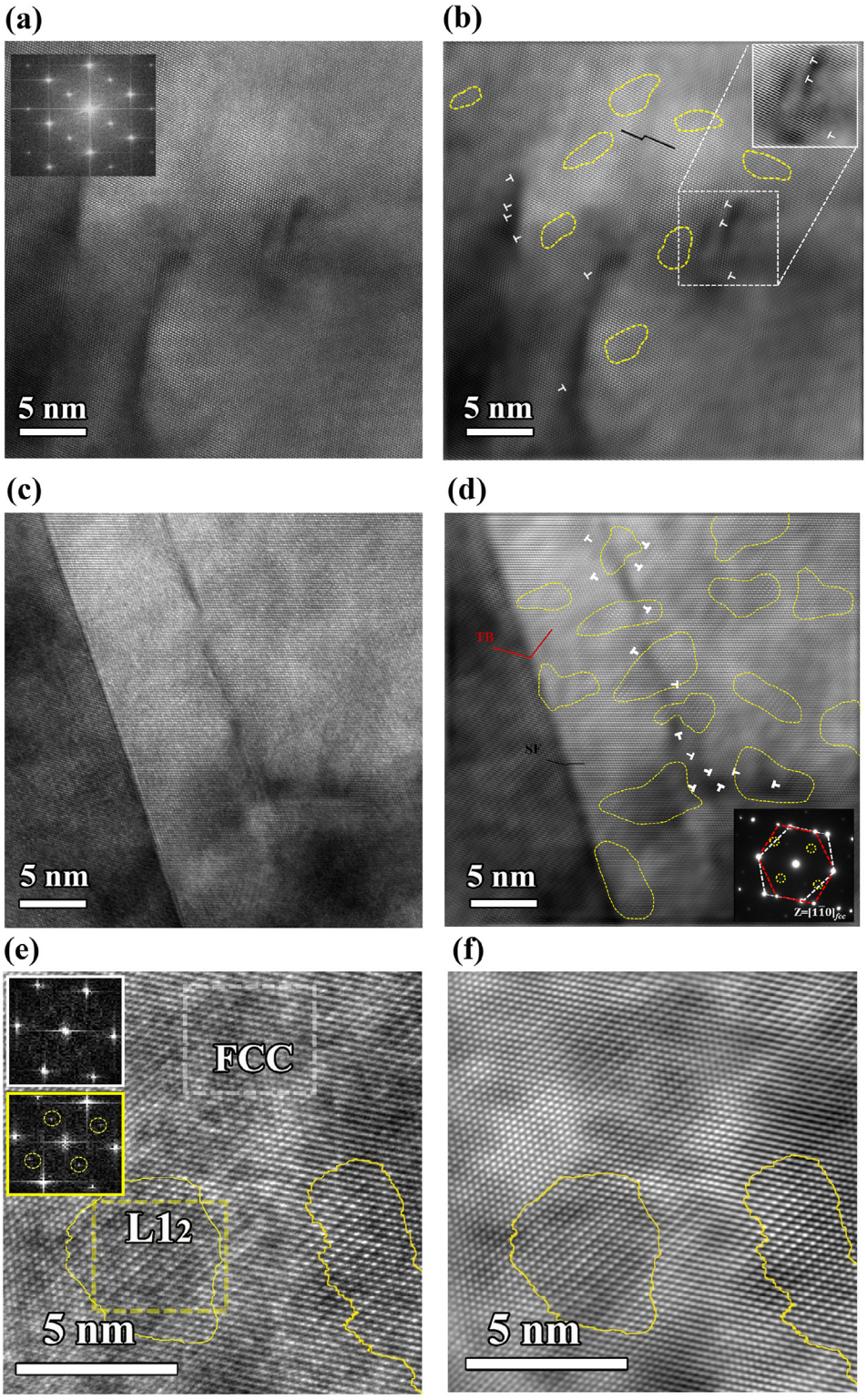

Fig. 8 – HRTEM images for typical samples after deformation at the same shear strain level ($\gamma = 1.2$). For 1000-Unaged sample: (a) HRTEM image (the FCC and $L1_2$ phases are indicated by the inset after FFT), (b) the corresponding image after FFT and inverse FFT. For 1000-Aged specimen: (c) HRTEM image, (d) the corresponding image after FFT and IFFT (the inset shows the twin relationship). (e) Close-up view of the coherent interface between $L1_2$ precipitate and FCC matrix, (f) the corresponding image after FFT and IFFT. $L1_2$ particles are highlighted by the dashed yellow outlines and the dislocations are marked by "T".

volume fraction for nano-sized $L1_2$ particles have a positive contribution on the activation energy for the planar dislocation slip.

The effects of $L1_2$ nanoprecipitate on the dynamic mechanical properties and the deformation mechanisms within the shear zone are also analyzed by the HRTEM, by which the interactions between $L1_2$ nanoprecipitate and dislocation are unveiled. The detailed deformation microstructures of the 1000-Unaged and 1000-Aged specimens at the same shear strain level 1.2 were examined by HRTEM. The HRTEM images and the corresponding images after fast Fourier transform (FFT) and inverse FFT (IFFT) are presented in Fig. 8. It is observed earlier that the aged specimen possesses a high-volume fraction of $L1_2$ nanoprecipitate as compared to the corresponding unaged one, suggesting that the aging treatment can considerably accelerate the nucleation and growth of $L1_2$ phase, which is consistent with the previous observations in Fig. 2. Moreover, the $L1_2$ phase shares the coherent interface with the FCC matrix, thus the lattice mismatch between these two phases is extremely small, which is well consistent with the XRD results in Fig. 1(a). For clarity, the close-up HRTEM images of the interfacial region are displayed in Fig.8(e) and (f), revealing the fully coherent boundary between $L1_2$ phase and FCC matrix. Remarkably, the higher density of dislocation is visible in the aged specimen as compared to the unaged one after dynamic deformation, as shown in Fig.8(c) and (d). It is also found that the $L1_2$ nanoprecipitates are frequently sheared by the dislocations, providing the pronounced precipitate strengthening/hardening contribution. Due to the coherent interface, the strain localization can be moderately relieved. Meanwhile, according to the glide plane softening model, the segmentation of nanoparticles could further facilitate the development of planar dislocation slip. In addition, the stacking faults and twins are also observed in the deformation structures for the 1000-Aged sample.

Based on the above discussions, it is therefore concluded that the better dynamic properties in the aged samples can be attributed to the presence and the higher volume fraction of coherent $L1_2$ nanoprecipitate, which play a dominant role in the triggered planar dislocation slip, the higher density of stored dislocations, the formation of dislocation substructure and the pronounced precipitation strengthening/hardening.

3.4. *Characterization of ASB*

3.4.1. *Phase transformation*

As the shear strain increases, the adiabatic shear localization becomes severer, especially in the corners of the hat-shaped specimen, as indicated in Fig. 6. The highest strain/stress state is preferentially developed around the corners during the dynamic plastic deformation, as indicated by previous simulation [65]. For the 1000-Unaged specimen under a high level of shear strain (approximately 2.1), it is worth noting that the volume fraction of B2 phase is found to increase significantly near the region of the upper or bottom corner as compared to the initial un-deformed state, as presented in Fig. 9 (a)–(c). The relative volume fraction of B2 phase around corners after shear deformation is estimated to be about 12%, which is much larger than that (5%) for the sample prior to dynamic shear deformation. Meanwhile, the corners of 1000-Unaged and 1000-Aged specimens under the 0.7 and 1.2

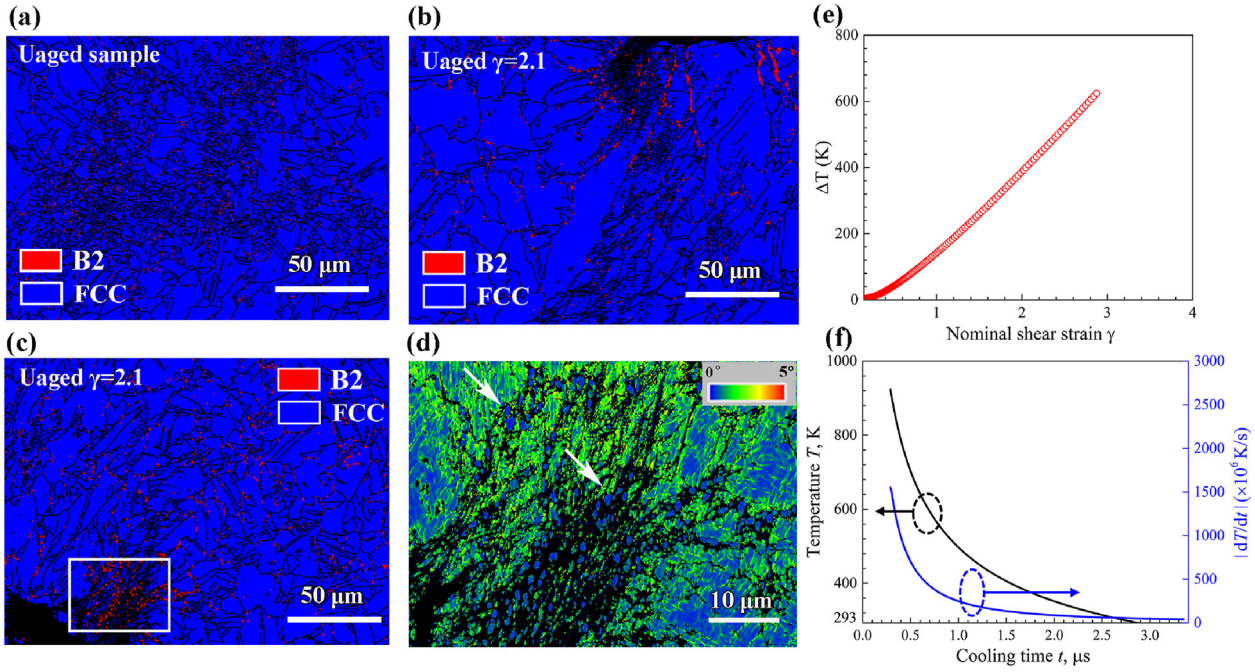

Fig. 9 – Microstructural characterization of the 1000-Unaged specimen. (a) EBSD phase maps for the initial undeformed state. (b) and (c) Phase distributions around the upper and lower corners of the hat-shaped specimen at the shear stain of 2.1. (d) Close-up view of KAM map from the square area in (c), and the newly formed B2 phase is indicated by the white arrows. (e) Temperature evolution in the shear zone as a function of time. (f) Temperature and fast-cooling rate curves in the shear zone as a function of time.

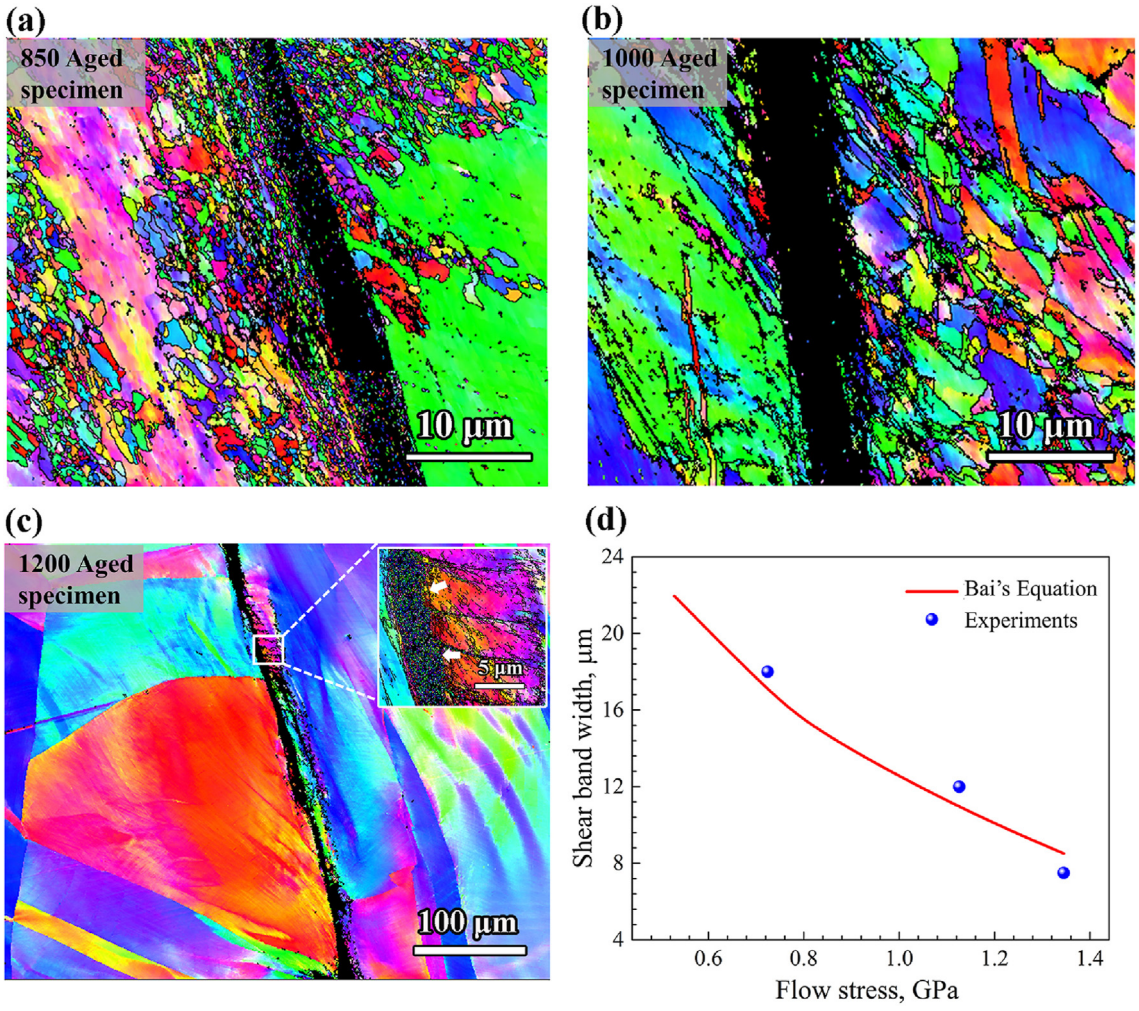

Fig. 10 – EBSD images showing the adiabatic shear bands for (a) 850-Aged, (b) 1000-Aged, and (c) 1200-Aged specimens, respectively. (d) The experimental width of ASB as a function of flow stress, in comparison with the estimation by the Bai's equation [9].

shear strains are also examined, and no extra B2 particles are formed. Additionally, the close-up view in Fig. 9(d) shows that the newly formed B2 particles have a larger grain size than that of the initial state, as well as a lower KAM value (marked with arrows) as compared to the surrounding sharply deformed regions. It is reasonable to deduce that the transformation from the disordered FCC phase to the ordered B2 phase is strongly dependent on the dynamic shear strain, as confirmed by a large amount of B2 phase formed at the corners of the hat-shaped specimen along the shear direction.

It is well accepted that the adiabatic shear localized deformation is associated with the high-temperature rise. The temperature rises ΔT can be estimated by [9].

$$\Delta T = \frac{\beta}{\rho C_p}\int \tau d\gamma \tag{5}$$

where ρ is the density (7.678 g/cm^3), C_p is the heat capacity (0.489 J/(g·K)), β represents the fraction of plastic work converted to heat-generation (β = 0.9). For the 1000-Unaged specimen, the temperature increases with the increasing shear strain, and eventually reaches up to nearly 600 °C within the shear zone, suggesting that the thermal softening effect gradually becomes dominant. It should be noted that the calculation of temperature rise by Eq. (5) is based on the assumption of uniform shear deformation in the shear zone, while the real temperature rise in the shear band after the formation of ASB should be even higher. In addition, with the assumption of a constant rate of heat generation in the shear zone, the cooling times for the center of the shear zone can be estimated by [66].

$$T(t) = \frac{w\Delta T}{\sqrt{4\pi kt/\rho C_p}} \tag{6}$$

where t is the cooling time, w represents the width of ASB, k is the thermal conductivity. It takes approximately 2 μs for the temperature in the shear zone to cool down to ambient temperature, as shown in Fig. 9(f). Therefore, the extremely high temperature within the localized region combined with the fast-cooling or quenching process may induce the precipitation of B2 phase, which is similar to the phase transformation from the austenite phase to B2 precipitates in the FeNiAlC alloy after the aging treatment [67]. It is thus concluded that the

transformation from FCC to B2 phases can be ascribed to the high strain/temperature state and the fast-cooling process. This newly observed phase transformation can be only fulfilled under high-strain-rate dynamic deformation, which was not observed under quasi-static deformation conditions before.

3.4.2. *Thickness of ASB*

As discussed earlier, the predicated temperature in the shear zone is higher than the temperature of recrystallization (about $0.4T_m$, T_m is the melting temperature of the alloy taken as 1600 K), meanwhile, the fast-cooling rate may effectively retain the deformed microstructures in the ASB. Thus, the microstructures of ASB for several aged specimens are examined and displayed in Fig. 10. It is found that the ASB is fully developed due to the sharply localized deformation, as indicated by the unidentified dark regions. In addition, the shear band widens with the increasing annealing temperature, presumably due to the postponed thermal softening effect in the coarse-grained specimen. Remarkably, equiaxed recrystallized nanograins are observed inside the shear band, as shown in the inset of Fig. 10(c), which provides evidence of dynamic recrystallization occurring within the shear band.

The width of ASB can be evaluated by the Bai and Dodd formula [9].

$$w = 2\left(\frac{kT}{\tau_* \dot{\gamma}_*}\right)^{1/2} \tag{7}$$

where the subscript (*) denotes the state inside the ASB. Generally, the shear strain rate $\dot{\gamma}_*$ is almost an order of magnitude higher than the experimental strain rate [38]. Hence, the width of ASB as a function of shear stress is displayed in Fig. 10(d). Increasing flow stress leads to a decrease in the width of ASB, which is in good agreement with the experimental observations. Meanwhile, it is revealed that the adiabatic shear band is strongly dependent on the grain size, in other words, the small grain size may be effective on prohibiting the propagation of ASB.

4. Conclusions

In this work, the dynamic shear responses of a high entropy alloy with dual-heterogeneous structures (heterogeneous grain structures and nanoprecipitate) are systematically investigated by hat-shaped specimens in the SHPB tests. The microstructural evolutions in the shear zone are examined by the controlled shear strain tests. The main findings are summarized as follows:

1. The present HEA with heterogeneous structures shows a superior combination of dynamic shear strength and nominal shear strain, which is better than all competitive metals and alloys tested before. Moreover, the aged samples with a higher volume fraction of coherent $L1_2$ nanoprecipitate display even better dynamic shear properties, as compared to the unaged samples.
2. The superior dynamic shear properties in the unaged samples can be attributed to the dynamical grain refinement, the dislocation hardening as well as the precipitation hardening for postponing the occurrence of ASB. The coherent $L1_2$ nano-particle is frequently sheared by the dislocations, contributing to the shearing strengthening/hardening. Meanwhile, dislocations bow out and bypass the B2 particles, leading to the Orowan-type strengthening/hardening. The even better dynamic shear properties in the aged samples should be due to the triggered planar dislocation slip, the stored higher density of dislocations, the formation of dislocation substructure, and the more pronounced precipitation hardening by the higher volume fraction of coherent $L1_2$ nanoprecipitate.
3. The phase transformation from FCC to B2 phases and the dynamic recrystallization are observed within ASB, associated with the high strain/temperature state and the fast-cooling process. This newly observed phase transformation can be only fulfilled under high-strain-rate dynamic deformation, which is not observed under quasi-static deformation conditions before.
4. The predicted widths of ASB are in good agreement with the experimental observations. The present findings should provide insights for applications of HEAs or MEAs with heterogeneous structures under extreme impact conditions.

Declaration of Competing Interest

The authors declare that they have no known competing financial interests or personal relationships that could have appeared to influence the work reported in this paper.

Acknowledgements

This research was supported by the National Key R&D Program of China [grant number 2017YFA0204402]; the NSFC Basic Science Center Program for “Multiscale Problems in Nonlinear Mechanics” [grant number 11988102], the National Natural Science Foundation of China [grant number 11790293], and the fellowship of China Postdoctoral Science Foundation [grant number 2021M703292].

REFERENCES

[1] Meyers MA, Subhash G, Kad BK, Prasad L. Evolution of microstructure and shear-band formation in α-hcp titanium. Mech Mater 1994;17:175–93.
[2] Liao S, Duffy J. Adiabatic shear bands in a TI-6Al-4V titanium alloy. J Mech Phys Solid 1998;46:2201–31.
[3] Wei Q, Kecskes L, Jiao T, Hartwig KT, Ramesh KT, Ma E. Adiabatic shear banding in ultrafine-grained Fe processed by severe plastic deformation. Acta Mater 2004;52:1859–69.
[4] Rittel D, Landau P, Venkert A. Dynamic recrystallization as a potential cause for adiabatic shear failure. Phys Rev Lett 2008;101:165501.
[5] Yuan FP, Jiang P, Wu XL. Annealing effect on the evolution of adiabatic shear band under dynamic shear loading in ultrafine-grained iron. Int J Impact Eng 2012;50:1–8.
[6] Sun K, Yu X, Tan C, Ma H, Wang F, Cai H. Influence of adiabatic shear bands intersection on the ballistic impact of Ti–6Al–4V alloys with three microstructures. Mater Sci Eng, A 2014;606:257–67.

[7] Guo Y, Ruan Q, Zhu S, Wei Q, Chen H, Lu J, et al. Temperature rise associated with adiabatic shear band: causality clarified. Phys Rev Lett 2019;122:015503.
[8] Guo Y, Liu R, Arab A, Zhou Q, Guo B, Ren Y, et al. Dynamic behavior and adiabatic shearing formation of the commercially pure titanium with explosion-induced gradient microstructure. Mater Sci Eng, A 2022;833:142340.
[9] Dodd B, Bai Y, Bai Y, editors. Adiabatic shear localization: frontiers and advances. 2nd ed. Amsterdam ; Boston: Elsevier; 2012.
[10] Yang Y, Jiang L. Self-organization of adiabatic shear bands in ZK60 Magnesium alloy. Mater Sci Eng, A 2016;655:321–30.
[11] Yan N, Li Z, Xu Y, Meyers MA. Shear localization in metallic materials at high strain rates. Prog Mater Sci 2021;119:100755.
[12] Bian XD, Yuan FP, Zhu YT, Wu XL. Gradient structure produces superior dynamic shear properties. Mater Res Lett 2017;5:501–7.
[13] Zhang W, He L, Lu Z, Kennedy GB, Thadhani NN, Li P. Microstructural characteristics and formation mechanism of adiabatic shear bands in Al–Zn–Mg–Cu alloy under dynamic shear loading. Mater Sci Eng, A 2020;791:139430.
[14] Zhu YT, Liao XZ. Retaining ductility. Nat Mater 2004;3:351–2.
[15] Yeh JW, Chen SK, Lin SJ, Gan JY, Chin TS, Shun TT, et al. Nanostructured high-entropy alloys with multiple principal elements: novel alloy design concepts and outcomes. Adv Eng Mater 2004;6:299–303.
[16] Cantor B, Chang ITH, Knight P, Vincent AJB. Microstructural development in equiatomic multicomponent alloys. Mater Sci Eng, A 2004;375–377:213–8.
[17] Schuh B, Mendez-Martin F, Völker B, George EP, Clemens H, Pippan R, et al. Mechanical properties, microstructure and thermal stability of a nanocrystalline CoCrFeMnNi high-entropy alloy after severe plastic deformation. Acta Mater 2015;96:258–68.
[18] Lei ZF, Liu XJ, Wu Y, Wang H, Jiang SH, Wang SD, et al. Enhanced strength and ductility in a high-entropy alloy via ordered oxygen complexes. Nature 2018;563:546–50.
[19] Jo YH, Jung S, Choi WM, Sohn SS, Kim HS, Lee BJ, et al. Cryogenic strength improvement by utilizing room-temperature deformation twinning in a partially recrystallized VCrMnFeCoNi high-entropy alloy. Nat Commun 2017;8:15719.
[20] Miao J, Slone CE, Smith TM, Niu C, Bei H, Ghazisaeidi M, et al. The evolution of the deformation substructure in a Ni-Co-Cr equiatomic solid solution alloy. Acta Mater 2017;132:35–48.
[21] Yang MX, Yan DS, Yuan FP, Jiang P, Ma E, Wu XL. Dynamically reinforced heterogeneous grain structure prolongs ductility in a medium-entropy alloy with gigapascal yield strength. Proc Natl Acad Sci USA 2018;115:7224–9.
[22] Sohn SS, Silva AK da, Ikeda Y, Körmann F, Lu WJ, Choi WS, et al. Ultrastrong medium-entropy single-phase Alloys designed via severe lattice distortion. Adv Mater 2019;31:1807142.
[23] Ding J, Yu Q, Asta M, Ritchie RO. Tunable stacking fault energies by tailoring local chemical order in CrCoNi medium-entropy alloys. Proc Natl Acad Sci U S A 2018;115:8919–24.
[24] Gludovatz B, Hohenwarter A, Catoor D, Chang EH, George EP, Ritchie RO. A fracture-resistant high-entropy alloy for cryogenic applications. Science 2014;345:1153–8.
[25] Gludovatz B, Hohenwarter A, Thurston KVS, Bei HB, Wu ZG, George EP, et al. Exceptional damage-tolerance of a medium-entropy alloy CrCoNi at cryogenic temperatures. Nat Commun 2016;7:10602.
[26] Valiev RZ, Alexandrov IV, Zhu YT, Lowe TC. Paradox of strength and ductility in metals processed bysevere plastic deformation. J Mater Res 2002;17:5–8.
[27] Wu XL, Zhu YT. Heterogeneous materials: a new class of materials with unprecedented mechanical properties. Mater Res Lett 2017;5:527–32.
[28] Fang TH, Li WL, Tao NR, Lu K. Revealing extraordinary intrinsic tensile plasticity in gradient nano-grained copper. Science 2011;331:1587–90.
[29] Wu XL, Jiang P, Chen L, Yuan FP, Zhu YT. Extraordinary strain hardening by gradient structure. Proc Natl Acad Sci USA 2014;111:7197–201.
[30] Wu XL, Yang MX, Yuan FP, Wu GL, Wei YJ, Huang XW, et al. Heterogeneous lamella structure unites ultrafine-grain strength with coarse-grain ductility. Proc Natl Acad Sci U S A 2015;112:14501–5.
[31] Zhang SD, Yang MX, Yuan FP, Zhou LL, Wu XL. Extraordinary fracture toughness in nickel induced by heterogeneous grain structure. Mater Sci Eng, A 2022;830:142313.
[32] Yang MX, Pan Y, Yuan FP, Zhu YT, Wu XL. Back stress strengthening and strain hardening in gradient structure. Mater Res Lett 2016;4:145–51.
[33] Zhu YT, Wu XL. Perspective on hetero-deformation induced (HDI) hardening and back stress. Mater Res Lett 2019;7:393–8.
[34] Yang Y, Chen TY, Tan LZ, Poplawsky JD, An K, Wang YL, et al. Bifunctional nanoprecipitates strengthen and ductilize a medium-entropy alloy. Nature 2021;595:245–9.
[35] Ming KS, Bi XF, Wang J. Realizing strength-ductility combination of coarse-grained Al0.2Co1.5CrFeNi1.5Ti0.3 alloy via nano-sized, coherent precipitates. Int J Plast 2018;100:177–91.
[36] Zhang ZH, Wang W, Qin S, Yang MX, Wang J, Jiang P, et al. Dual heterogeneous structured medium-entropy alloys showing a superior strength-ductility synergy at cryogenic temperature. J Mater Res Technol 2022;17:3262–76.
[37] Yang T, Zhao YL, Liu WH, Kai JJ, Liu C. L12-strengthened high-entropy alloys for advanced structural applications. J Mater Res 2018;33:2983–97.
[38] Ma Y, Yuan FP, Yang MX, Jiang P, Ma E, Wu XL. Dynamic shear deformation of a CrCoNi medium-entropy alloy with heterogeneous grain structures. Acta Mater 2018;148:407–18.
[39] Pu Z, Chen Y, Dai LH. Strong resistance to hydrogen embrittlement of high-entropy alloy. Mater Sci Eng, A 2018;736:156–66.
[40] Liu XF, Tian ZL, Zhang XF, Chen HH, Liu TW, Chen Y, et al. "Self-sharpening" tungsten high-entropy alloy. Acta Mater 2020;186:257–66.
[41] Li Z, Zhao S, Alotaibi SM, Liu Y, Wang B, Meyers MA. Adiabatic shear localization in the CrMnFeCoNi high-entropy alloy. Acta Mater 2018;151:424–31.
[42] Qin S, Yang MX, Jiang P, Yuan FP, Wu XL. Excellent tensile properties induced by heterogeneous grain structure and dual nanoprecipitates in high entropy alloys. Mater Char 2022;186:111779.
[43] Meyer LW, Manwaring S. Metallurgical applications of shock-wave and high-strain-rate phenomena, vols. 657–674. Cambridge University Press; 1987.
[44] Zhang ZH, Jiang P, Yuan FP, Wu XL. Enhanced tensile properties by heterogeneous grain structures and coherent precipitates in a CoCrNi-based medium entropy alloy. Mater Sci Eng, A 2022;832:142440.
[45] Manzoni AM, Haas S, Yu JM, Daoud HM, Glatzel U, Aboulfadl H, et al. Evolution of γ/γ' phases, their misfit and volume fractions in Al10Co25Cr8Fe15Ni36Ti6 compositionally complex alloy. Mater Char 2019;154:363–76.
[46] Forbord B, Hallem H, Ryum N, Marthinsen K. Precipitation and recrystallisation in Al–Mn–Zr with and without Sc. Mater Sci Eng, A 2004;387–389:936–9.
[47] Wang S, Chen S, Jia Y, Hu Z, Huang H, Yang Z, et al. FCC-L12 ordering transformation in equimolar FeCoNiV multi-principal element alloy. Mater Des 2019;168:107648.
[48] Liang YJ, Wang LJ, Wen YR, Cheng BY, Wu QL, Cao TQ, et al. High-content ductile coherent nanoprecipitates

achieve ultrastrong high-entropy alloys. Nat Commun 2018;9:4063.
[49] Recht RF. Catastrophic thermoplastic shear. J Appl Mech 1964;31:189–93.
[50] Wei Q. Strain rate effects in the ultrafine grain and nanocrystalline regimes—influence on some constitutive responses. J Mater Sci 2007;42:1709–27.
[51] Meyers MA, Mishra A, Benson DJ. Mechanical properties of nanocrystalline materials. Prog Mater Sci 2006;51:427–556.
[52] Tsai KY, Tsai MH, Yeh JW. Sluggish diffusion in Co–Cr–Fe–Mn–Ni high-entropy alloys. Acta Mater 2013;61:4887–97.
[53] Xue Q, Gray GT, Henrie BL, Maloy SA, Chen SR. Influence of shock prestraining on the formation of shear localization in 304 stainless steel. Metall Mater Trans A 2005;36:1471–86.
[54] Xing JX, Yuan FP, Wu XL. Enhanced quasi-static and dynamic shear properties by heterogeneous gradient and lamella structures in 301 stainless steels. Mater Sci Eng, A 2017;680:305–16.
[55] Yuan FP, Bian XD, Jiang P, Yang MX, Wu XL. Dynamic shear response and evolution mechanisms of adiabatic shear band in an ultrafine-grained austenite–ferrite duplex steel. Mech Mater 2015;89:47–58.
[56] Xue Q, Gray GT. Development of adiabatic shear bands in annealed 316L stainless steel: Part I. Correlation between evolving microstructure and mechanical behavior. Metall Mater Trans A 2006;37:2435–46.
[57] Pushkov V, Yurlov A, Bol'shakov A, Podurets A, Kal'manov A, Koshatova E. Study of adiabatic localized shear in metals by split Hopkinson pressure bar method. EPJ Web Conf 2010;10:00029.
[58] Pushkov VA, Yurlov AV, Podurets AM, Tsibikov AN, Tkachenko MI, Balandina AN. Effect of preloading on the formation of adiabatic localized shear in copper. Combust Explos Shock Waves 2013;49:620–4.
[59] Hofmann U, El-Magd E. Behaviour of Cu-Zn alloys in high speed shear tests and in chip formation processes. Mater Sci Eng, A 2005;395:129–40.
[60] Gu YB, Nesterenko VF. Dynamic behavior of HIPed Ti–6Al–4V. Int J Impact Eng 2007;34:771–83.
[61] Kubin LP, Mortensen A. Geometrically necessary dislocations and strain-gradient plasticity: a few critical issues. Scripta Mater 2003;48:119–25.
[62] Zhao S, Li Z, Zhu C, Yang W, Zhang Z, Armstrong DEJ, et al. Amorphization in extreme deformation of the CrMnFeCoNi high-entropy alloy. Sci Adv 2021;7:3108–37.
[63] Zhao YL, Li YR, Yeli GM, Luan JH, Liu SF, Lin WT, et al. Anomalous precipitate-size-dependent ductility in multicomponent high-entropy alloys with dense nanoscale precipitates. Acta Mater 2022;223:117480.
[64] Welsch E, Ponge D, Hafez Haghighat SM, Sandlöbes S, Choi P, Herbig M, et al. Strain hardening by dynamic slip band refinement in a high-Mn lightweight steel. Acta Mater 2016;116:188–99.
[65] Budiwantoro B, Kariem MA, Febrinawarta B. The influence of shear angles on the split Hopkinson shear bar testing. Int J Impact Eng 2021;149:103787.
[66] Nemat-Nasser S, Isaacs JB, Liu M. Microstructure of high-strain, high-strain-rate deformed tantalum. Acta Mater 1998;46:1307–25.
[67] Ma Y, Zhou LL, Yang MX, Yuan FP, Wu XL. Ultra-high tensile strength via precipitates and enhanced martensite transformation in a FeNiAlC alloy. Mater Sci Eng, A 2021;803:140498.